# Removal of a Cationic Dye from Aqueous Solution Using Lignosulfonate–Graphene Oxide–Polyaniline Ternary Nanocomposite: Investigation of Adsorption Parameters

## Shammala FA*

Department of Chemistry, Faculty of Pharmacy, University of Palestine, Palestine

***Corresponding author:** Farid Abu Shammala, Adjunct Professor, Faculty of Pharmacy, University of Palestine, Gaza, Palestine, Email: drfaridshammala@hotmail.com

## Abstract

This study explores the removal of malachite green (MG); as examples of hazardous cationic dye pollutants, from aqueous solution by a novel lignosulfonate–graphene oxide–polyaniline (LS-GO-PANI) nanocomposite. LS-GO-PANI consist of three dimentional graphite polymer structure decorated with a number of oxygen containing functionalities such as carboxyl, epoxy, ketone, and hydroxyl groups, and a secondary amine negative charge Q -N-Q-N- Q where Q represents the benzenoid ring from the polyaniline which impart a negative charge density to it in aqueous solution at a wide range of pH. The kinetics of the adsorption data were analyzed using various adsorption models such as Langmuir, Freundlich, and Tempkin were used for the experimental isotherms data. Kinetic and isotherm studies revealed that the Langmuir adsorption isotherm data fit well with the experimental adsorption data compared to the other two models. The adsorption capacity of LS-GO-PANI nanocomposite for MG was found to be 345.4 mg/g, the adsorption maximum was reached after 120 min and follows the linear form of pseudosecond-order kinetics. The adsorption isotherm of adsorption has been investigated in the pH range of 2 to 9 at 298K. Various thermodynamic parameters such as the Gibbs free energy ($\Delta G°$), enthalpy ($\Delta H°$), and entropy ($\Delta S°$) change were also evaluated. The negative value of $\Delta G$ indicates spontaneity of the adsorption process of the malachite green (MG) on LS-GO-PANI nanocomposite.

**Keywords:** Graphene Oxide; Lignosulfonate; Polyaniline; Malachite Green; Cationic Dye; Nanocomposites; Adsorption

## Introduction

Ancient dyes were all natural with the dyestuffs coming from a variety of natural sources, extracted from shells, flowers, roots, insects and molluscs. But, now days with the historic discovery of first synthetic dye, Mauveine, most of the uses of natural dyes have been replaced with synthetic ones as they can be manufactured on a large scale. Synthetic dyes usually have a complex aromatic molecular structure, which possibly comes from coal-tar based hydro-carbons such as benzene, naphthalene, toluene, xylene, etc. The complex aromatic molecular structures of dyes make them more stable and more difficult to biodegrade [1]. Textile, paper, plastics, and cosmetic industries use a wide variety of dyes to color their products and discharge large amount of effluents including dyes which are very toxic and could cause serious ecological problems. Therefore, dye pollution in water stream is a major environmental problem [2].

Indeed, at the present time, more than 1,00,000 synthetic

dyes exist with an annual production of over $7 \times 10^5$ tonnes/year and are mostly associated with water pollution [3-5]. Malachite green (MG) is water soluble cationic dye that appears as green crystalline powder and belongs to triphenylmethane category [6]. The extensive usage of MG dye has caused several health hazards problem and hence, proper treatment technology to decolorization of MG dye is extremely urgent.

Indeed, many technologies have been applied for treatment of effluent containing MG from aqueous medium, such as biodegradation and decolorization [7-34]; photocatalytic degradation[35]; photooxidative degradation [36]; Solar degradation [37]; coagulation–flocculation [38,39]; ozonation [40]; fenton reagent [41,42]; Solvent extraction [43]; sonochemical and sonophotocatalytic degradation [44-46]. However, all these techniques have certain limitations and drawbacks in terms of design, dye separation efficiency, cost and effectiveness.

Recently, carbon based nanomaterials have been established themselves as excellent adsorbents for treatment of dyes from aqueous solutions, include graphite, nanotubes, nanoparticles, nanofibers, nanorods, fullerenes, and nanowires [47-51]. Carbon nanotubes were discovered accidentally by Iijima [52], while studying the surfaces of graphite electrodes used in an electric arc discharge. CNTs are divided into two types based on the arrangement of their graphene cylinders: (1) single-walled CNTs (SWCNTs) and (2) multi-walled CNTs (MWCNTs) [53,54]. MWNTs are collections of several concentric graphene cylinders and are larger structures compared to SWNTs which are individual cylinders of 1–2 nm diameter. The former can be considered as a mesoscale graphite system, whereas the latter is truly a single large molecule [55]. Indeed, the mechanisms by which the dye molecules are sorbed onto CNTs are very complicated and appear attributable to electrostatic attraction, sorption, precipitation and chemical interaction between the reactive groups of dye molecules and the surface functional groups of CNTs. Recently, Rajabi, et al. [56] functionalized MWCNTs with the carboxylate group and used as an adsorbent for the rapid and fast removal of MG dye from the aqueous solutions. The optimized contact time and pH were 10 min and 9, respectively. The effect of temperature revealed that the adsorption capacity of MG dye increased with increasing contact time, temperature and pH. The adsorption equilibrium and kinetic data was well fitted and found to be in good agreement with the Langmuir isotherm model and pseudo second order kinetic model, respectively. Shirmardi, et al. [57] prepared functionalized multi-walled carbon nanotubes (f-MWCNTs) by acid treatment and used for the adsorption of MG dye from aqueous solution in batch mode. The results indicated that by increasing contact time, pH and adsorbent dosage, the removal percentage increased, but by increasing the initial MG concentration, the removal percentage decreased. Based on correlation coefficient ($R^2$), the experimental data follows the Langmuir isotherm with maximum adsorption capacity of 142.85 mg/g. Halloysite, a mineral of the kaolin group [forms hollow tubular crystals (halloysite nanotubes—HNTs)], can be used as MG dye adsorbent by Kiani, et al. [58] and found that the equilibrium adsorption was reached within 30 min. The adsorption of MG by HNTs obeyed pseudo-second-order kinetics with activation energy 18.28 kJ/mol, suggested that the process was physisorption. The best-fit adsorption isotherm was achieved with the Langmuir model, indicating that homogeneous adsorption occurred. The negative values of $\Delta G°$ and positive value of $\Delta H°$ showed that the adsorption was a spontaneous and endothermic. The particles of at least one dimension smaller than 1 µm, and potentially as small as atomic and molecular length scales (0.2 nm) are called nanoparticles. Nanoparticles can have amorphous or crystalline form [59]. Thus, due to the unique characteristics such as small size, catalytic potential, large surface area, ease of separation, and large number of active sites for interaction with different contaminants the nanomaterials have considered as excellent adsorbents [6].

Lignosulfonates, are water-soluble anionic polyelectrolyte polymers, are byproducts from the production of wood pulp using sulfite pulping [60]. Lignosulfonates have a wide variety of applications such as plasticizers in making concrete, production of plasterboard, disperse pesticides, dyes, carbon black, tanning leather. They are also used to suppress dust on unpaved roads, and used as binders in well-paper, particle boards, linoleum flooring, coal briquettes, and roads [60]. This molecule contains a large amount of sulfate, carboxyl and hydroxyl functional groups that can complex metal ions [61]. Therefore, sodium alginate can also be used as a medical antidote for treating heavy metal ion poisoning [62]. However, alginate aerogels have poor mechanical properties. After repeated use, the aerogel structure can be easily destroyed, thereby resulting in an unstable adsorption capacity for heavy metal ions [63]. This kind of material shows improved mechanical properties given its special adhesion. In addition, Polyaniline (PANI) is a conducting polymer of the semi-flexible rod polymer family The major applications are printed circuit board manufacturing: final finishes, antistatic and ESD coatings, and corrosion protection [64]. Polyaniline and its derivatives are also used as the precursor for the production of N-doped carbon materials through high-temperature heat treatment [65]. Polyaniline with two types of functional groups (sulfonated poly(aniline-co-o-aminophenol), s-copolymer) has been prepared by the electrochemical copolymerization of aniline and o-aminophenol in sulfuric acid solution followed by sulfonation of the copolymer in the concentrated sulfuric acid [65].

The main objective of this work, was to synthesized new adsorbents nanohybrid materials composed of graphene oxide (GO), lignosulfonate, and polyaniline (LS-GO-PANI) to fully eliminate the MG dye from aqueous solutions under different experimental conditions (solution pH, contact time and amount of adsorbent). The innovative nanohybrid nanomaterial was characterized by different techniques. Optimum conditions, dynamics, and thermodynamics for the eradication of the MG dye were also investigated [66].

## Materials and Methods

### Reagents and Chemicals

The entire chemical used in this study were prepared from Sigma Aldrich (St. Louis, Mo, USA) and Merck (KGaA, Darmstadt, Germany) and used without modification and without further purification. Natural graphite powder (325 mesh, purity of 99.95%), lignosulfonate (low viscosity, LS, $C_{20}H_{24}Na_2O_{10}S_2$, MW 534.51), vitamin C (VC, purity of 99.5%), polyaniline, nitric acid (HNO3), sodium hydroxide (NaOH), metal salts, $Pb(NO_3)_2$, $K_2Cr_2O_7$, and other reagents were of analytical grade. MG, a model of cationic dyes with a molecular formula of $C_{23}H_{25}N_2Cl$ [67]. The MG used in the present study has a molecular weight of 364.911 with its maximum absorbance at a wavelength of 624 nm. Distilled water was used for the preparation of dye solutions. All solutions were prepared by using ultrapure water. The pH value of the solution was adjusted with 1.0 M $HNO_3$ or NaOH [68].

### Instrumentation Measurements

FT-IR spectra were conducted on a Vertex 70 instrument (Bruker, Rheinstetten, Germany) at a resolution of 0.5 cm⁻¹, and in the range of 500 cm⁻¹ to 4000 cm⁻¹. The atomic force microscope (AFM, Nanoscope III Veeco Co. Ltd., Santa Barbara, USA) was obtained to characterize the GO samples. Samples for AFM analysis were prepared on freshly cleaved mica. The X-ray diffraction (XRD) patterns of dried samples were measured with a Bruker D8 Advance diffractometer. The conditions of test were: the tube current and voltage at 20 mA and 30 kV, respectively, Cu target (λ = 0.15418 nm), and data were collected from the 2θ angular regions between 5° and 60°. The thermal stability of the dried samples was employed investigated using a TGA Q500 (TA Instruments, New Castle DE, USA). The samples were heated in an aluminum crucible to 650°C at a heating rate of 20°C/min. Surface morphology of dried samples was analyzed by scanning electron microscopy (SEM; Bruker) at 10 kV. The samples for SEM analysis were coated with a thin layer of gold (2 nm) by sputtering to promote conductivity before SEM observation. To observe the nitrogen adsorption isotherms at -196°C, ASAP 2460 instrument was employed. The specific surface area was evaluated from the adsorption branch of the isotherm using Brunauer-Emmett-Teller theory (BET). The X-ray photoelectron spectroscopy (XPS) was performed on a Axis Ultra DLD spectrometer (Kratos, Manchester, UK) with monochrome Al Kα radiation (hν = 1486.6 eV). A JJ-1 electric agitator (Changzhou Guohua Company, Changzhou, China) and MS7-H550-Pro agitator (Dragon Laboratory Instruments Limited, Beijing, China) were used for mechanical and magnetic stirring, respectively. A PHS-3E acidity meter was used to determine the pH value of the solution. The concentration of Pb(II) and Cr(VI) after adsorption was measured using atomic absorption spectrophotometer (Z-2000, Hitachi Ltd., Tokyo, Japan).

### Synthesis of Graphene Oxide

Graphene oxide (GO) was synthesized from natural graphite powder according to the procedures described by Hummers's method. Inorder to avoid aggregation of the GO during drying process, the GO sample was obtained first by freeze-drying. Then dried GO sample was dispersed in water by using ultrasonication for 1 h to get an aqueous dispersion at a concentration of 2.0 mg/mL. were prepared

### Synthesis of the Nanocomposite (LS-GO-PANI)

The adsorbent (LS-GO-PANI) was prepared as follows. First, 2.0 g of alginosulfate was weighed and dissolved in 98.0 mL of ultrapure water. Second, VC (20 g), and GO aqueous dispersion (200 mL) were added to a 500 mL glass flask. The reaction mixture was stirred at room temperature until it became a stable suspension. The aqueous dispersions of the LS, VC, and GO were then heated at 60°C, the solution and mechanically stirred for 3 hours. Third, 2.0 g of polyaniline was added to the mixture, and stirring was continued for 12 hours at room temperature, and the ternary nanocomposite were then collected by filtration and washed thrice with ultrapure water. Fourth, the hydrogels were immersed in ultrapure water, placed in a vacuum freeze-drying apparatus, frozen for 4 hours, and vacuum dried for 20 hours to obtain the lignosulfonate–graphene oxide–polyaniline (LS-GO-PANI) nanocomposite aerogel [69].

### Adsorption and Desorption Tests

A stock solution of MG (1.0 g/L) was prepared by dissolving 1g of MG powder in 1L of double distilled water. The desired concentrations ranging from 10 to 60 mg/L were obtained by dilution. For each adsorption experiment, 50 ml of the dye solution with a specified concentration was stirred at 100 rpm in a glass flask. The pH of solutions was adjusted to a desired value by adding 0.1 mol/L NaOH or HCl solution. Batch adsorption experiments were carried out using a thermostated shaker for a certain contact time with LS-GO-PANI nanocomposite at a determined temperature at 100 rpm. At predetermined time intervals, samples were withdrawn by a pipette and centrifuged at 4000 rpm.

Then, the residual concentration was determined from a constructed calibration curve by measuring the absorbance at batch adsorption experiments were carried out to examine effects of adsorbent dosage, initial dye concentration, solution pH, and time on the adsorption of MG on LS-GO-PANI nanocomposite. The amount of MG adsorbed on LS-GO-PANI nanocomposite (at a predetermined time t), qt (in mg/g), was determined using the mass balance equation:

$$q_t = (C_o - C_t) \times m / v \ldots\ldots\ldots (1)$$

The decolorization rate (η) of MG was calculated by the following equation:

$$\mu = (C_o - C_t) / C_o \times 100\% \ldots\ldots\ldots (2)$$

Where $C_0$ is the initial concentration of MG (in mg/L), $C_t$ (in mg/L) is the instant concentration of MG at a predetermined time t, V is the volume of the solution (in L), and m is the mass LS-GO-PANI nanocomposite (in g).

In an adsorption experiment, About 100 mg of LS-GO-PANI nanocomposite was weighed and added to 100 mL of the 0.1 mM of MG solution, loaded in a 200 mL conical flask and placed it in an air table with 200 rpm stirring speed at 25°C for 24 hours to reach equilibrium. The desired pH value was adjusted using 0.1 M HCl or 0.1 M NaOH solution and eventually filtered through filter paper and a funnel at atmospheric pressure. The nanocomposite was immersed in 50 mL of the 0.05 M $HNO_3$ solution for 30 minutes, filtered, and washed thrice with ultrapure water, and the amount of MG remaining in the filtrate was measured using the UV-Vis spectrophotometer at maximum absorbance wavelength of 624 nm.

## Results and Discussion

### TEM Images

The morphologies and structures of GO and LS-GO-PANI nanocomposite were observed by TEM and SEM, respectively. TEM images of nano-graphene oxide (GO) (Figure 1a), and graphite oxide with LS-GO-PANI nanocomposite are illustrated (Figure 1b). The specific surface area values of GO and LS-GO-PANI were examined by Brunauer–Emmett–Teller (BET) analysis Majid [66] and the results are shown that the values of the specific surface area and the pore size of the GO were 64.32 $m^2$ $g^{-1}$ and 0.2392 $cm^3$ $g^{-1}$, respectively. The values of specific surface area and the pores size of the LGPH were 110.44 $m^2$ $g^{-1}$ and 0.2839 $cm^3$ $g^{-1}$, respectively [31-33]. The BET surface area of LS-GO-PANI is larger than GO due to the surface of LS-GO-PANI being rougher than MGO, after GO was modified using LS and PANI which is also seen in the TEM images for GO and LS-GO-PANI (Figure 1). As the figures indicate, graphene oxide has a plate structure and the LS and PANI are penetrated and spread over the grapheme oxide plates.
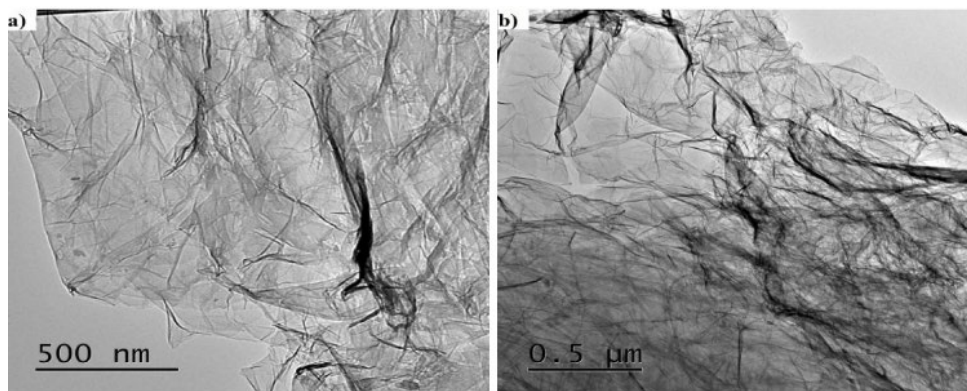


**Figure 1:** TEM images of (a) grapheme oxide (GO), (b) lignosulfonate–graphene oxide–polyaniline (LS-GO-PANI) nanocomposite.

### SEM Images

Figure 2a, 2b are a depicts the SEM images of GO and LS-GO-PANI, the morphology and microstructure of monolith were analyzed by scanning electron microscopy (SEM-S420, HITACHI) equipped with a field-emission electron gun. The SEM image of GO (Figure 2a) a depicts a typical flake-like morphology, agglomerated into a two-dimensional multilayered structure with a smooth surface and lateral sizes of several nanometers, which demonstrates the large specific surface area of GO. The diverse layers can overlap and interweave with each other to form the bright and shaded areas on the GO surface. In Figure 2b, SEM images of the LS-GO-PANI nanocomposites are showcased A much rougher surface and more wrinkled structure are found in the LS-GO-PANI image, and yet, the

image was very similar to the GO SEM image. The cross-sectional analysis showed that the thickness of the GO sheets were in the ranges of 0.98 nm, which illustrated that the GO sheet was about one-atom-thick graphene oxide. SEM images results of freeze-dried samples of LS-GO-PANI indicated a well-defined and interconnected 3D porous network as revealed by. It is depicted that PANI and LS assembles on the surface of GO sheets. The π-π stacking of GO sheets plays an important role in the formation 3D network porous structure. SEM analysis exhibited formation of interconnected 3D morphology and it can be noted that incorporation of LS and PANI with GO brought significant change in pore wall thickness and shrinkage in average size compared to those of GO. High magnification SEM image of hybrid samples showed the presence of needle-like LS and

PANI in random direction which behave as compact skeleton within the dense and wrinkling type graphene sheets. Thus, it can be inferred that these surface decorated/adsorbed LS and PANI may promote roughness between adjacent graphene sheets that results in compact 3D assembly due to strong chemical interaction. Furthermore, the results of the LS-GO-PANI nanocomposite indicaes the π-π conjugation and hydrogen bonding between graphene sheets and LS and PANI contributed to the successful construction of 3D porous structure [33-35]. Thus, favoring the accumulation and adsorption of Pb(II) and Cr(VI) ions from aqueous samples . Moreover, the multilevel pore structure of LS-GO-PANI provided large specific surface area (473.5 $m^2/g$) that was higher than that of GO (261.7 $m^2/g$). These findings were also confirmed by the nitrogen adsorption-desorption isotherms
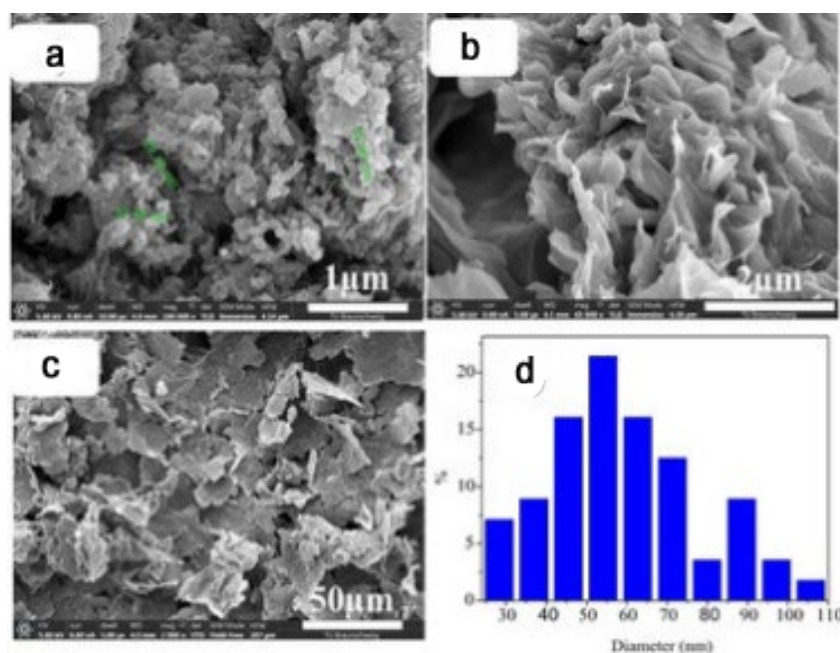


**Figure 2:** SEM images of (a) Graphite oxide (GO), (b, c) graphite oxide with lignosulfonate and polyaniline nanocomposite LS-GO-PANI (d) particle size distribution histogram of LS-GO-PANI.

## Elemental Analysis and Mapping of Phases

The elemental distribution mapping performed in order to find different elements and their distribution in the synthesized samples, energy dispersive X-ray (EDX) analysis was accomplished as seen in Figure 3. The EDX spectrum of GO shows C and O as the main component while the composite materials showcase all the elements of GO, PANI and LS, including C, O, S and N. The % weight of N and O atoms, respectively, decreases and increases with an increasing GO percentage. The presence of a high amount of S in the synthesized samples suggests effective incorporation of the

LS in the structure of the nanocomposite. Consequently, the results indicated that the specific surface area of LS-GO-PANI was larger than that of GO, improving the adsorption capacity to metal ion. Thus, the large surface area of LS-GO-PANI contributes to the high adsorption capacity during the hydrothermal reaction. LS and PANI incorporated into graphene sheets through both covalent and non-covalent interactions, such as π-π conjugation and hydrogen bonding. The negatively charged LS molecules spread in the interlayer of graphene oxide sheets, thus prevents the restacking of graphene sheets through electrostatic repulsion.
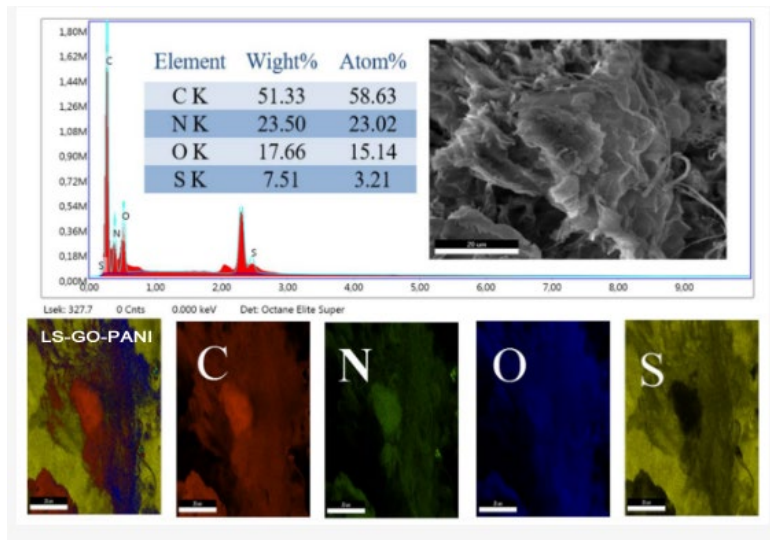
**Figure 3**: Elemental analysis and mapping of LS-GO-PANI -nanocomposite.

## AFM Image and Thickness

Atomic force microscope was performed to examine the in three-dimensional topography of our samples, and to provides various types of surface measurements.
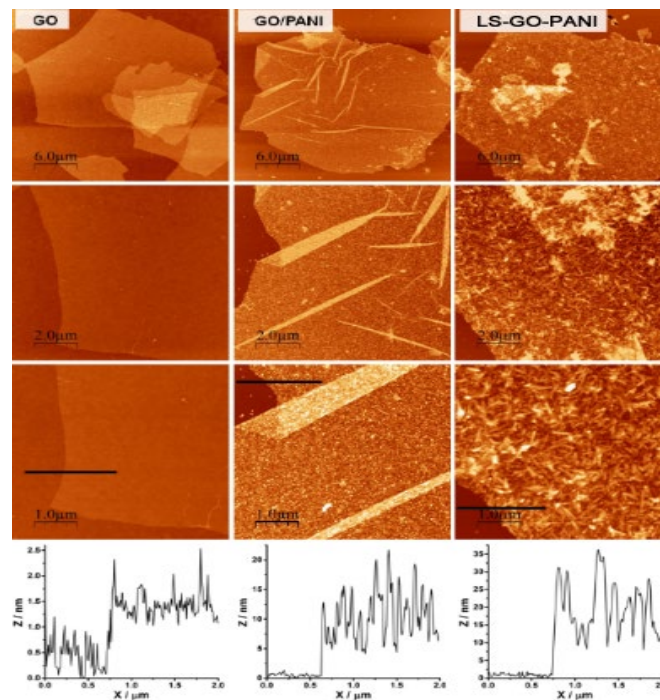


**Figure 4:** AFM images of GO, GO-LS and LS-GO-PANI nanocomposites at different scan sizes (30, 10 and 5 μm), and height profiles (thicknesses) (for the 5 μm scan size images) nanoplatelets measured from AFM image.

Figure 4 shows the morphology and thickness of LS-GO-PANI nanocomposite by AFM. Figure 4 shows that LS-GO-PANI nanocomposite samples typically had flake-like and sheet-like structures with less than 1 μm lateral size and

the range of thickness of LGPH samples was between 1 to 3 nm. The layer-to-layer distance (d-spacing) of graphene oxide (GO) is 0.850 nm, which indicated that this LS-GO-PANI nanocomposite sample typically has 1 to 3 layers. The lateral size of LGPH was typically less than 1 μm, which was less than that of graphene oxide (GO) made from natural graphene. The sonication can exfoliate the LS-GO-PANI to fewer layers, and the nanoscaled LS-GO-PANI nanocomposite may apply for conductive materials [70].

## FTIR Images

FTIR spectra of the different samples have been recorded as presented in Figure 5 a and b. The successful oxidation of graphene oxide was confirmed in Figure 4a, by the presence of various kinds of oxygen functionality such as peak at 3129-3440 $cm^{-1}$ which are mainly originated from the stretching vibration of hydroxyl group (-OH). The peaks attributed to the deformation vibration of the tertiary (C-OH) groups appeared at 1400 $cm^{-1}$. The peaks at 1598 $cm^{-1}$ for carboxylic group (-C=O), the bands located at 1620-1630 $cm^{-1}$ resulted from the (C=C) stretching mode of the graphitic domains. The peaks located at approximately 1225 and 1080 $cm^{-1}$ correspond to the stretching vibrations of (C-O-C) and (C-O), respectively. The peaks at 1218 $cm^{-1}$ for epoxy (C-O) stretching and alkoxy (C-OH) stretching at 1043 $cm^{-1}$. The peaks located at approximately 1225 and 1080 $cm^{-1}$ correspond to the stretching vibrations of (C-O-C) and (C-O), respectively. In addition, the peaks attributed to the

deformation vibration of the tertiary C-OH groups appeared at 1400 $cm^{-1}$. These hydrophilic groups on the surface are very important to improve the interaction between LS, PANI and GO sheets. As shown in Figure 4b the FT-IR spectra of LS-GO-PANI nanocomposites, the peak at 3440-3129 $cm^{-1}$ was due to the O–H stretching. The bands around 1350-1342 $cm^{-1}$ are attributed to sulfonic acid groups. The bands between 839 and 608 $cm^{-1}$ was due to the C-S stretching vibration. The characteristic peaks at 3213 $cm^{-1}$ and 1598 $cm^{-1}$ belonging to GO can also be observed in the spectra of GO and LS-GO-PANI. Interestingly, spectra in Figure 3b showed shifting of the functional groups such as carboxyl band (C=O) from 1721 $cm^{-1}$ to carboxylic starching 1727 $cm^{-1}$ which confirmed the successful reaction between GO, LS and PANI after treatment. This indicated that there exist a certain number of functional groups on reduced GO sheets. The characteristic peaks at 1635 and 1567 $cm^{-1}$ are attributed to the stretching vibration of quinoid and benzenoid rings on PANI molecular chain. The characteristic peak at 1417 $cm^{-1}$ is corresponding to the stretching mode of N-Q-N where Q represents the benzenoid ring Additionally, compared with the GO, the S=O symmetric stretching at 1023 cm-1 belonging to LS was also observed, which indicated the proposed formation of LGPH. The existences of sulfonic acid groups were evident from the FTIR spectra and these groups were responsible for improving its adsorption capacity to water and metal ions. The change at 3129-3440 $cm^{-1}$ could be ascribed to the strong interaction through hydrogen bonds and π-π conjugation between LS and GO sheets [71].
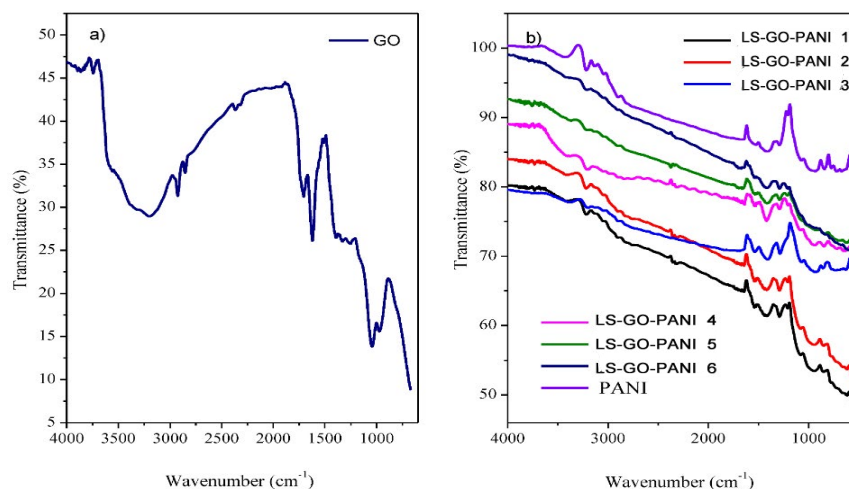


**Figure 5:** FT-IR spectra of (a) porous graphene oxide GO and (b) PANI and different samples of LS-GO-PANI nanocomposites.

This phenomenon is suggesting that the presence of LS and PANI plays important role for the self-assembly of monolithic material and promotes chemical interaction force, presumably, hydrogen bonding as evident from

shifting of these functional groups, since we failed to obtain 3D monolith in the absence of LS and PANI. However, nature of hydrogen bonding between bare graphene sheets and/or between GO sheets and LS follows different routes. Compared

to control sample, hybrid spectrum exhibits downshifting at starching vibration of hydroxyl (OH), carboxyl (C-O, C-O-C), and N-H bending vibration mode. This shift can be seen as synergy effect of strong hydrogen bonding between graphene sheets and LS, thus greatly influencing the microstructure morphology and mechanical and thermal properties of hybrid material. It can be inferred that strong chemical interaction between GO, PANI and LS is predominantly influenced by C=O···HO and N-H···OH type hydrogen bonding during the hydrothermal treatment. Moreover, shrinkage in OH starching was due to deoxygenation of graphene.

## Raman Spectra

The structural characterisation of PANI, GO-PANI and LS-GO-PANI nanocomposites were performed by Raman spectroscopy, as presented in Figure 6. Raman bands in the spectra of PANI, GO/PANI and LS-GO-PANI at 632.8 nm excitation wave lengths are mainly attributed to the polymer due to resonance effects with the polaronic/bipolaronic electronic transitions of PANI, and the high content of polymer in these materials. The spectra presented in Figure 6a show the characteristic features of the PANI polymer for all samples. However, comparing the spectra of the nanocomposites with the neat polymer (PANI), the bands at ca. 1336 and ca. 1600 cm$^{-1}$ for the hybrid materials present higher relative intensities. These results can be attributed to the contribution of GO bands, and changes in the doping state of the polymer due to interaction with the LS and PANI components.
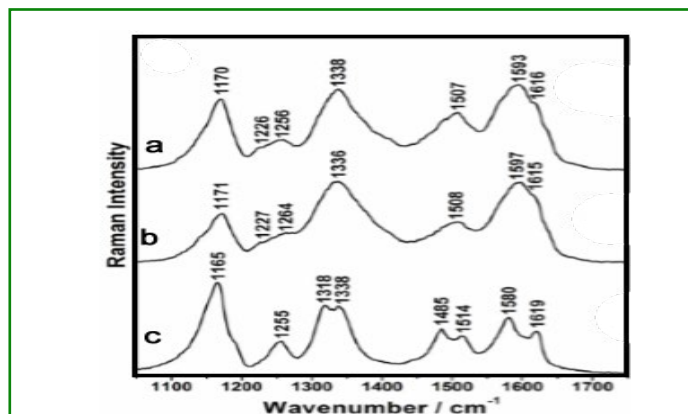


**Figure 6:** Raman spectra (λ0 = 632.8 nm) of (a) LS-GO-PANI, (b) GO/PANI and (c) PANI in the range of 1050–1750 cm$^{-1}$.

## XRD Patterns

Figure 7 XRD spectra of (a) GO, (b) lignosulfonate (LS), (c) PANI, and (d) LS-GO-PANI nanocomposite. The GO pattern (Figure 6a) showed a peak at ~10.7° corresponding to the (001) inter-planar spacing of 8.30 Å which caused by the

oxygen-rich groups on both sides of the sheets and the water molecules trapped between the GO sheets. The calculated interlayer spacing of the freeze-dried GO and LS-GO-PANI nanocomposite was observed to be 3.69 Å, and 3.65 Å, respectively. This value was much lower than that of GO (8.30 Å), which suggested the presence of π-π stacking between graphene sheets in the composites and also the presence of a certain number of functional groups on reduced GO sheets. For GO spectra, the reduced GO sheets can encapsulate water in the process of self-assembly due to the presence of residual hydrophilic oxygenated groups. For LS-GO-PANI, in addition to functional groups on reduced GO sheets, the hydrophilic groups of LS and PANI could also capture a multitude of water molecules. Because of this factor and the stacking of graphene sheets, the composites can be successfully synthesized by one-step method. Lignosulfonate (LS) XRD spectra shows a broad peak between 20° and 30° was attributed to its low graphitization and amorphous nature. Furthermore, there has been obvious distinction between the XRD patterns of GO, LS and LS-GO-PANI, which indicated that LS was chemically reacted on GO surface. Moreover, there has been obvious similarity between the XRD patterns of PANI and LS-GO-PANI nanocomposite [72].
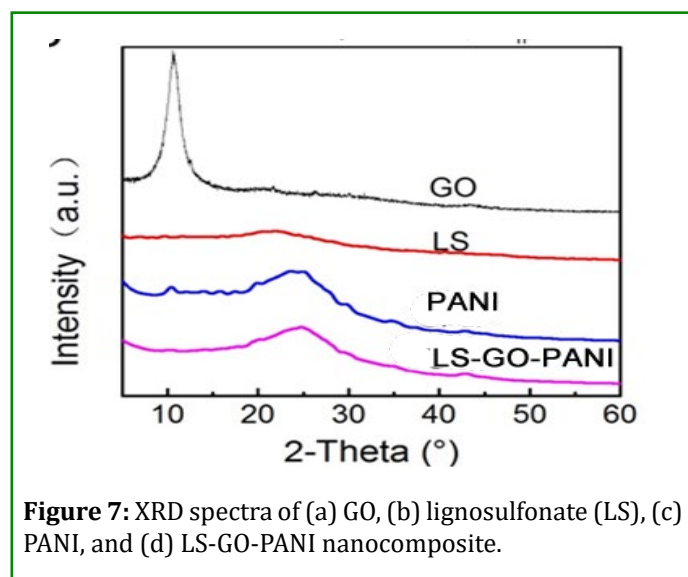


**Figure 7:** XRD spectra of (a) GO, (b) lignosulfonate (LS), (c) PANI, and (d) LS-GO-PANI nanocomposite.

## XPS Patterns

High-resolution XPS spectra can also provide information on the reduction degree of GO, since C 1s core level photoelectrons present slightly different binding energies depending on the environment of the carbon atoms. Figure 8 shows the high-resolution XPS spectra at the C 1s core level for GO and rGO samples prepared by reactions at 25 °C for 7 days and at 80 °C for 3. XPS spectra of GO and rGO consist mainly of two asymmetric and highly overlapping peaks (maxima at ca. 285 and ca. 287 eV). The comparison of these spectra clearly

shows the increase of relative intensity of the low-binding energy peak upon reduction. This is attributed to the partial recovery of the sp2-hybridized carbons in the graphene structure, since pristine graphite presents only an asymmetric peak at ca. 284 eV (carbon atoms in sp2 environment). The curve fitting of the C 1s spectra, also presented in Figure 8, can provide detailed information on the oxygen-containing groups, since these groups induce different environments for the carbon atoms and, consequently, their corresponding C 1s photoelectrons present slightly different binding energies. The comparison of the curve fitting for GO and rGO-25 shows the increase of the contribution from sp2 carbons (C=C) and hydroxy groups (C–OH) upon reduction, and the decrease of sp3 carbons (C–C + C–H) and epoxy groups (C–O–C). These results are in good agreement with the literature

and indicate the recovery of the sp2 carbon atoms from the sp3 carbon atoms and epoxy groups, and the conversion of some epoxy to hydroxy groups. In contrast, rGO presents a dramatic change in the C 1s spectral profile, evidenced by an intense peak at ca. 284 eV and a weak shoulder at 285–290 eV. The comparison of the curve fitting for this sample and rGO shows a significant increase of the contribution from the sp2 carbon atoms and decrease of the contribution from sp3 carbon atoms, hydroxy and epoxy groups. These features are very similar to data reported in literature for chemically reduced GO and indicate a high degree of reduction of the rGO sample. This also points out the very important role of the temperature on the recovery of the sp2 carbon network in graphene oxide [73].
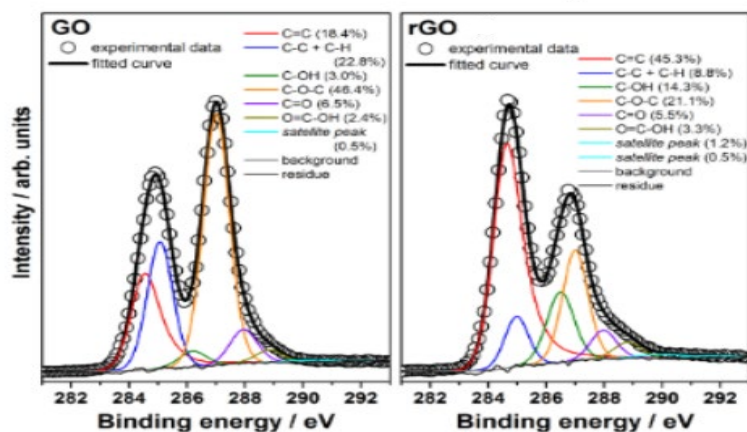


**Figure 8:** XPS spectra at the C 1s core level of GO and rGO samples prepared by reactions at 25°C for 7 days or at 80°C for 3 h.
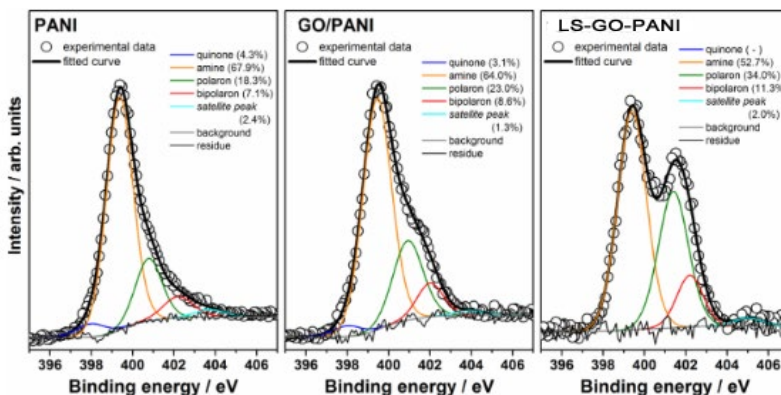


**Figure 9:** XPS spectra at N 1s core level of (a) PANI, (b) GO/PANI and (c) LS-GO-PANI nanocomposite.

Figure 9 shows XPS spectra at the N 1s core level of PANI, GO/PANI and LS-GO-PANI nanocomposite, and the respective curve fitting results. Analogously to C 1s, XPS spectra at the N 1s core level can be discussed in detail and

provide interesting structural information on the GO/PANI and LS-GO-PANI nanocomposite. In the present work, the N 1s peaks are mostly from nitrogen-containing groups of PANI, the amine, imine or charged nitrogen sites of the

polymeric chains. Therefore, XPS spectroscopy provides important information on the oxidation and doping states of the polymer in PANI-based materials. The N 1s peak of PANI-based materials is dominated by an amine (–NH–)-related component at ca. 399 eV, but also shows components of quinone (=N–), polaron (–N•+H–) and bipolaron (=N+H–) groups at ca. 398, ca. 401 and ca. 402 eV, respectively. The comparison of spectral data for PANI and rGO/PANI in Figure 9 indicate that PANI chains present a higher doping state in the presence of GO flakes. XPS data for the LS-GO-PANI nanocomposite clearly shows a significant increase in the relative intensity of the peak with higher biding energy. These results clearly indicate that LS nanoparticles also play an important role to the increase of the doping state of PANI.

## Effect of Adsorbent Dosage

The results in Figure 10 has shown that adsorption of MG in the solution by LS-GO-PANI nanocomposite is greatly affected by the dose of adsorbent used. A range of adsorbent dose from 0.01 to 0.07 g was used with 20 ml of 10, 50, and 100 mg $L^{-1}$ of MB solution for 120 min to investigate the effect of dose on removal of MB, and the results are shown in Figure 10. It was found that the adsorption efficiency increases as the amount of adsorbent increase up to 0.04 g, but on further increasing the adsorbent dose, the adsorption capacity decreases. This result is expected because of the increased adsorbent surface area and availability of more adsorption sites caused by increasing adsorbent dosage. This trend can be explained as the adsorbent dose increases, the number of adsorbent particles also increases facilitating more active sites for adsorption but on further increase in adsorbent dose adsorption capacity decreases due to partial aggregation of adsorbent particles. Thus, 0.04 g was taken as optimum adsorbent dose for all the experiments.
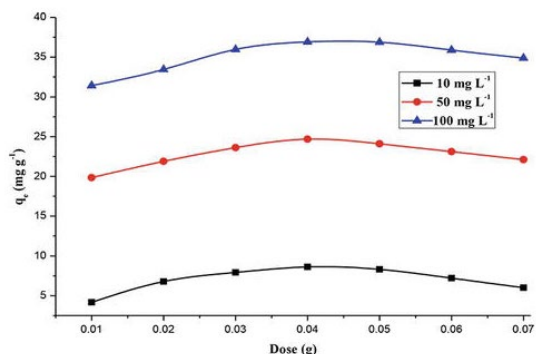
**Figure 10:** Effect of adsorbent dose on adsorption of MG on LS-GO-PANI nanocomposite at 10, 50, and 100 mg $L^{-1}$ initial metal ion concentrations.

## Effect of Solution pH

One the most important parameter that directly affects the adsorption of MG is pH of the solution. The effect of the initial solution pH on the removal of MG was studied with 0.05 g of LS-GO-PANI nanocomposite, 20 ml of 10, 50, and 100 mg $L^{-1}$ MG solution with different pH in the range 2–7 at 30°C. The effect of pH on sorption of MG has been shown in Figure 6. It was found that the maximum adsorption capacity for MG was in the pH value of 2 and as the pH value increases the adsorption capacity decreases.
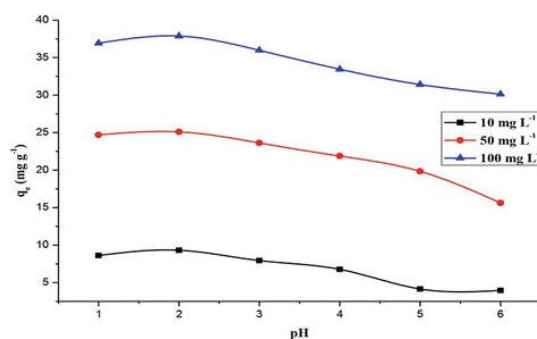
**Figure 11:** Effect of pH on adsorption of MG on LS-GO-PANI nanocomposite at 10, 50, and 100 mg $L^{-1}$ initial metal ion concentrations.

## Effect of Contact Time and Initial Metal ion Concentration

A 50 ml of 50 mg/L of MG dye was taken in conical flasks and treated with 0.1 gm LS-GO-PANI nanocomposite (adsorbent) at several times (30, 60, 90, 120, 180, 240 and 300 min.) the variation in percent removal of dye with the time was shown in Figure 12.
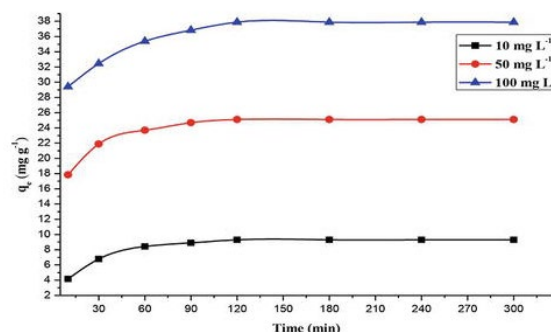
**Figure 12:** Effect of contact time on adsorption of MB on LS-GO-PANI nanocomposite at 10, 50, and 100 mg $L^{-1}$ initial metal ion concentration

The effect of retention time on removal efficiency of MG was carried out by varying the contact time in the range of 10–300 min at three different MG dye concentrations 10, 50, and 100 mg L$^{-1}$ at pH 2 at adsorbent dose of 0.04 g. The effect of contact time on LS-GO-PANI nanocomposite for MG removal is depicted in Figure 7 indicating an initial increase in adsorption capacity with increase in time and attaining the equilibrium time at 120 min after that little change in adsorption capacity for MG is seen which indicates that the system has already achieved equilibrium. No change in adsorption capacity after equilibrium reveals that the adsorption sites are completely occupied by metal ion. Thus, the equilibrium time 120 min was chosen as optimum time in subsequent experiments.

## Evaluation of Metal Ions Uptake Characteristics of LGPH Nanocomposite by the Adsorption Isotherms

After finding the optimum time, dosage, and pH of the metal ions, adsorption isotherm experiments were performed for the evaluation of the metal uptake mechanism and capacity. Various adsorption models such as Langmuir, Freundlich, and Tempkin were used for the experimental isotherms data as shown in Figure 13-14. The calculated isotherm parameters, correlation coefficient ($R^2$) values, and standard deviations in the measurement were used for the evaluation of the suitability of the isotherms and are summarized in Table 1. The Langmuir adsorption isotherm data fit well with the experimental adsorption data compared to the other two models. The adsorption parameters are summarized in Table 1. Hence, the adsorption of MG dye onto LS-GO-PANI nanocomposite was monolayer chemisorption on the homogeneous surface. The adsorption capacity of LS-GO-PANI nanocomposite was greater than that of GO alone due to the high electron transfer charge of LS-GO-PANI nanocomposite by LS. The maximum adsorption capacity of LS-GO-PANI nanocomposite at 298±2 K for MG dye was high, indicating LS-GO-PANI nanocomposite to be a promising and better adsorbent for heavy metal adsorption. It was also clearly observed from Table 1 that the adsorption capacity of LS-GO-PANI nanocomposite was higher than the GO indicates the synergistic enhancement of the adsorption MG dye by LS-GO-PANI nanocomposite. The high dsorption of LS-GO-PANI nanocomposite may be due to the fact that the LS-GO-PANI nanocomposite has a high surface area and high surface site density when compared with GO. The distribution of MB between the LS-GO-PANI nanocomposites in equilibrium over a range of concentrations at three different temperatures (298–328 K) was studied. From the Langmuir isotherm model, the calculated maximum adsorption capacities ($q_{max}$) were increased as the temperature increased from 298 to 328 K for both metal ions. The increasing adsorption capacity with increasing temperature is associated with endothermic adsorption of metal ions onto LS-GO-PANI nanocomposite

at equilibrium. Hence, the adsorption process was favorable and rapid
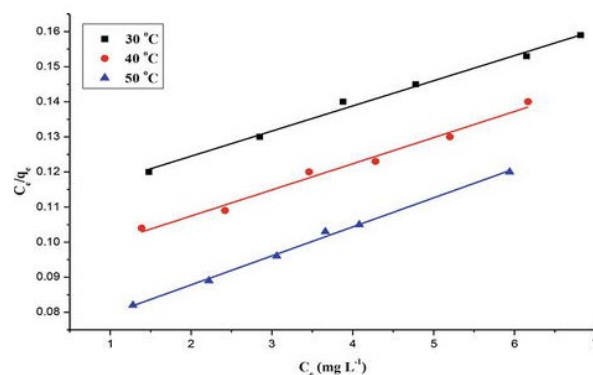


**Figure 13:** Langmuir adsorption isotherm for MG on LS-GO-PANI nanocomposite at 30, 40, and 50°C (dose = 0.04 g and pH = 2).
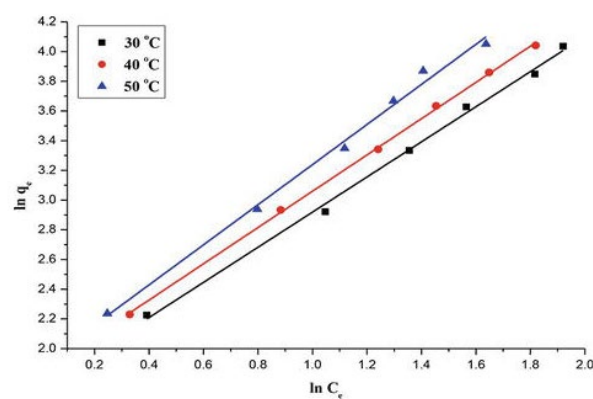


**Figure 14:** Freundlich adsorption isotherm for MG on LS-GO-PANI nanocomposite at 30, 40, and 50°C (dose = 0.04 g and pH = 2).
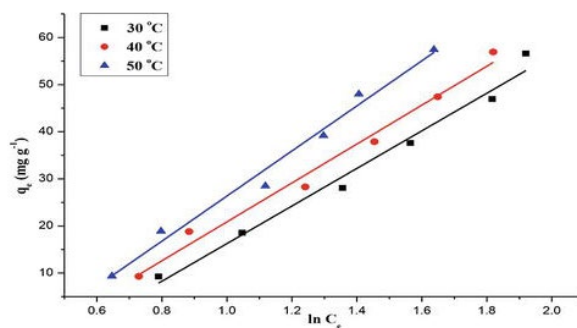


**Figure 15:** Temkin adsorption isotherm for MG on LS-GO-PANI nanocomposite at 30, 40, and 50°C (dose = 0.04 g and pH = 2)

| Dye | Composite | Langmiur | | | Freundlich | | | Temkin | | |
|-----|-----------|----------|----------|----------|----------|---|----------|----------|------|----------|
| | | $q_m$(mg/g) | $K_L$(L/mg) | $R^2$ | $K_F$(mg/g) | $n$ | $R^2$ | $K_T$(L/mg)n | B | $R^2$ |
| MB | LS-GO-PANI | 345.4 | 1.85 | 0.993 | 69.12 | 1.42 | 0.978 | 25.54 | 62.51 | 0.987 |
| MB | GO | 67.35 | 0.16 | 0.993 | 8.81 | 0.52 | 0.895 | 0.84 | 12.4 | 0.86 |

**Table 1:** Isotherm parameters of MG on LS-GO-PANI nanocomposite) (Co= 2.0 to 25 mg·L$^{-1}$) at 0.4 g·L$^{-1}$ dosage and 298 ±2 K for 30 min (n= 3, mean).

## Adsorption Thermodynamics

To substantiate our prediction about the endothermic nature of the adsorption process, thermodynamic parameters such as Gibbs free energy change ($\Delta G°$), enthalpy change ($\Delta H°$), and entropy change ($\Delta S°$) were calculated using the Gibbs equation and the Van't Hoff equation. The thermodynamic parameters associated with the MG adsorption by the LS-GO-PANI nanocomposite are listed in Table 2. The positive value of $\Delta H°$ confirmed the endothermic nature of the adsorption process of MB on LS-GO-PANI. The values of $\Delta G°$ are all negative, and the negative value of $\Delta G°$ increases as the temperature increase from 30 to 50°C, which indicates that the MG adsorption process of the nanocomposite is spontaneous and spontaneity increases with temperature. The positive value of $\Delta S°$ revealed the increased randomness and an increase in the degrees of freedom at the adsorbent-solution interface during the immobilization of the MG on the active sites of the adsorbent, which indicate the partial liberation of the salvation MG from solvent molecules before adsorption (liberation of water molecules from solvated- MG), therefore, enabling commonness of randomness and spontaneity in the system.

| Concentration | $\Delta H^0$ (KJ mol$^{-1}$) | $\Delta S^0$ (KJ mol-1 K-1) | $\Delta G^0$ (KJ mol-1) | | |
|---------------|------------------------------|------------------------------|-------|-------|-------|
| | | | **303K** | **313K** | **323K** |
| 10 mg L$^{-1}$ | 1.67 | 0.015 | -2.78 | -2.98 | -3.18 |
| 50 mg L$^{-1}$ | 3.89 | 0.025 | -2.9 | -3.38 | -3.35 |
| 100 mg L$^{-1}$ | 3.89 | 0.024 | -3.28 | -3.58 | -3.78 |

**Table 2:** Thermodynamic parameters for MG removal by LS-GO-PANI nanocomposite.

## Conclusion

A green novel approach to synthesis lignosulfonate–graphene oxide–polyaniline (LS-GO-PANI) porous hydrogel nanocomposite via solvothermal route and further investigated for the adsorptive removal of MG from aqueous solution. The modification of graphene composite with lignosulfonate (LS) improved its adsorption sites, resulting in excellent MB accumulation efficiency from aqueous solution. Kinetic and isotherm studies revealed that the Langmuir adsorption isotherm data fit well with the experimental adsorption data compared to the other two models. The adsorption capacity of LS-GO-PANI nanocomposite for MG was found to be 345.4 mg/g. Thermodynamic analysis suggested that the adsorption was spontaneous and endothermic in nature. MB adsorption was found to be high at acidic pH, and reached a maximum at pH 2.0.

## Conflicts of Interest

The authors declare no conflict of interest regarding the publication of this paper.

## References

1. Fewson CA (1988) Biodegradation of Xenobiotic and other Persistence Compounds: The causes of Recalcitrance. Trends Biotechnol 6(7): 148-153.

2. Perju MM, Dragon ES (2008) Removal of azo dyes from aqueous solution using chitosan. Chem Eng 137: 238-243.

3. Mittal A, Mittal J, Malviya A, Gupta VK (2009) Adsorptive removal of hazardous anionic dye "Congo Red" from wastewater using waste materials and recovery by desorption. J Colloid Interface Sci 340(1): 16–26.

4. Gupta VK, Jain R, Nayak A, Agarwal S, Shrivastava M (2011) Removal of the hazardous dye-tartrazine by photodegradation on titanium dioxide surface. Mater Sci Eng C 31(5): 1062-1067.

5. Saravanan R, Sacari E, Gracia F, Khan MM, Gupta VK, et al. (2016) Conducting PANI stimulated ZnO system for visible light photocatalytic degradation of coloured dyes. J Mol Liq 221: 1029-1033.

6. Raval NP, Shah PU, Ladha DG, Wadhwani PM, Shah NK (2016) Comparative study of chitin and chitosan beads for the adsorption of hazardous anionic azo dye Congo Red from wastewater. Desalin Water Treat 57(20): 9247-9262.

7. An SY, Min SK, Cha IH, Choi YL, Cho YS, et al. (2002) Decolorization of triphenylmethane and azo dyes by Citrobacter sp. Biotechnol Lett 24(12): 1037-1040.

8. Levin L, Papinutti L, Forchiassin F (2004) Evaluation of Argentinean white rot fungi for their ability to produce lignin-modifying enzymes and decolorize industrial dyes. Bioresour Technol 94(2): 169-176.

9. Eichlerová I, Homolka L, Nerud F (2006) Synthetic dye decolorization capacity of white rot fungus Dichomitus squalens. Bioresour Technol 97(16): 2153-2159.

10. Daneshvar N, Ayazloo M, Khataee AR, Pourhassan M (2007) Biological decolorization of dye solution containing malachite green by microalgae Cosmarium sp. Bioresour Technol 98(6): 1176-1182.

11. Ayed L, Chaieb K, Cheref A, Bakhrouf A (2008) Biodegradation of triphenylmethane dye Malachite Green by Sphingomonas paucimobilis. World J Microbiol Biotechnol 25(4): 705-711.

12. Ali H, Ahmad W, Haq T (2009) Decolorization and degradation of malachite green by Aspergillus flavus and Alternaria solani. Afr J Biotechnol 8(8): 1574-1576.

13. Wu J, Jung BG, Kim KS, Lee YC, Sung NC (2009) Isolation and characterization of Pseudomonas otitidis WL-13 and its capacity to decolorize triphenylmethane dyes. J Environ Sci China 21(7): 960–964.

14. Cheriaa J, Bakhrouf A (2009) Triphenylmethanes, malachite green and crystal violet dyes decolourisation by Sphingomonas paucimobilis. Ann Microbiol 59(1): 57-61.

15. Ayed L, Chaieb K, Cheref A, Bakhrouf A (2010) Biodegradation and decolorization of triphenylmethane dyes by Staphylococcus epidermidis. Desalination 260(1-3): 137-146.

16. Du LN, Wang S, Li G, Wang B, Jia XM, et al. (2011) Biodegradation of malachite green by Pseudomonas sp. strain DY1 under aerobic condition: characteristics, degradation products, enzyme analysis and phytotoxicity. Ecotoxicology 20(2): 438-446.

17. Khataee AR, Zarei M, Dehghan G, Ebadi E, Pourhassan M (2011) Biotreatment of a triphenylmethane dye solution using a Xanthophyta alga: modeling of key factors by neural network. J Taiwan Inst Chem Eng 42(3): 380-386.

18. Shedbalkar U, Jadhav JP (2011) Detoxification of malachite green and textile industrial effluent by Penicillium ochrochloron. Biotechnol Bioprocess Eng 16(1): 196–204.

19. Hu R, Huang JB, Yang ZP, Cheng ZZ, Jing DJ, et al. (2011) Biosorption of crystal violet and malachite green by Rhodotorula graminis Y-5. Ying Yong Sheng Tai Xue Bao J Appl Ecol Zhongguo Sheng Tai Xue Xue Hui Zhongguo Ke Xue Yuan Shenyang Ying Yong Sheng Tai Yan Jiu Suo Zhu Ban 22(12): 3293-3299.

20. Hasnat MA, Siddiquey IA, Saiful IS (2003) Photodegradation of malachite green in the aqueous medium. Indian J Chem Sect A 42(8): 1865-1867.

21. Kominami H, Kumamoto H, Kera Y, Ohtani B (2003) Photocatalytic decolorization and mineralization of malachite green in an aqueous suspension of titanium(IV) oxide nano-particles under aerated conditions: correlation between some physical properties and their photocatalytic activity. J Photochem Photobiol Chem 160(1-2): 99-104.

22. Lv X, Xu Y, Lv K, Zhang G (2005) Photo-assisted degradation of anionic and cationic dyes over iron(III)-loaded resin in the presence of hydrogen peroxide. J Photochem Photobiol Chem 173(2): 121-127.

23. Chen CC, Lu CS, Chung YC, Jan JL (2007) UV light induced photodegradation of malachite green on TiO2 nanoparticles. J Hazard Mater 141(3): 520-528.

24. Sayılkan F, Asiltürk M, Tatar P, Kiraz N, Arpaç E, et al. (2007) Photocatalytic performance of Sn-doped TiO2 nanostructured mono and double layer thin films for malachite green dye degradation under UV and vis-lights. J Hazard Mater 144(1-2): 140-146.

25. Sayılkan F, Asiltürk M, Tatar P, Kiraz N, Arpaç E, et al. (2007) Preparation of re-usable photocatalytic filter for degradation of malachite green dye under UV and vis-irradiation. J Hazard Mater 148(3): 735–744.

26. Tayade RJ, Surolia PK, Kulkarni RG, Jasra RV (2007) Photocatalytic degradation of dyes and organic contaminants in water using nanocrystalline anatase and rutile TiO2. Sci Technol Adv Mater 8(6): 455–462.

27. Wang Q, Chen C, Zhao D, Ma W, Zhao J (2008) Change of adsorption modes of dyes on fluorinated TiO2 and its effect on photocatalytic degradation of dyes under visible irradiation. Langmuir ACS J Surf Colloids 24(14):

7338–7345.

28. Ju Y, Yang S, Ding Y, Sun C, Zhang A, et al. (2008) Microwave-assisted rapid photocatalytic degradation of malachite green in TiO2 suspensions: mechanism and pathways. J Phys Chem A 112(44): 11172-11177.

29. Pan X, Zhang D (2009) Removal of malachite green from water by Firmiana simplex wood fiber. Electron J Biotechnol 12(4): 9-10.

30. Kaneva N, Stambolova I, Blaskov V, Dimitriev Y, Vassilev S, et al. (2010) Photocatalytic activity of nanostructured ZnO films prepared by two different methods for the photoinitiated decolorization of malachite green. J Alloys Compd 500(2): 252-258.

31. Bojinova A, Dushkin C (2011) Photodegradation of malachite green in water solutions by means of thin films of TiO2/WO3 under visible light. React Kinet Mech Catal 103(1): 239-250.

32. Chen Y, Zhang Y, Liu C, Lu A, Zhang W (2011) Photodegradation of malachite green by nanostructured Bi2WO6 visible light-induced photocatalyst. Int J Photoenergy 2012(1): 510-518.

33. Tolia J, Chakraborty M, Murthy Z (2012) Photocatalytic degradation of malachite green dye using doped and undoped ZnS nanoparticles. Pol J Chem Technol 14(2): 16–21.

34. Saha S, Wang JM, Pal A (2012) Nano silver impregnation on commercial TiO2 and a comparative photocatalytic account to degrade malachite green. Sep Purif Technol 89: 147-159.

35. Aliyan H, Fazaeli R, Jalilian R (2013) Fe3O4@ mesoporous SBA-15: a magnetically recoverable catalyst for photodegradation of malachite green. Appl Surf Sci 276: 147-153.

36. Modirshahla N, Behnajady MA (2006) Photooxidative degradation of malachite green (MG) by UV/H2O2: influence of operational parameters and kinetic modeling. Dyes Pigments 70(1): 54-59.

37. Pirsaheb M, Shahmoradi B, Khosravi T, Karimi K, Zandsalimi Y (2015) Solar degradation of malachite green using nickel-doped TiO2 nanocatalysts. Desalin Water Treat 57(21): 9881-9888.

38. Oladoja NA, Aliu YD (2009) Snail shell as coagulant aid in the alum precipitation of malachite green from aqua system. J Hazard Mater 164(2-3): 1496-1502.

39. Man LW, Kumar P, Teng TT, Wasewar KL (2012) Design of experiments for malachite green dye removal from wastewater using thermolysis—coagulation–flocculation. Desalin Water Treat 40(1-3): 260-271.

40. Zhou XJ, Guo WQ, Yang SS, Zheng HS, Ren NQ (2013) Ultrasonic-assisted ozone oxidation process of triphenylmethane dye degradation: evidence for the promotion effects of ultrasonic on malachite green decolorization and degradation mechanism. Bioresour Technol 128: 827-830.

41. Chen F, Ma W, He J, Zhao J (2002) Fenton degradation of malachite green catalyzed by aromatic additives. J Phys Chem A 106(41): 9485-9490.

42. Nidheesh PV, Gandhimathi R, Ramesh ST (2013) Degradation of dyes from aqueous solution by Fenton processes: a review. Environ Sci Pollut Res 20(4): 2099-2132.

43. Pandit P, Basu S (2004) Removal of ionic dyes from water by solvent extraction using reverse micelles. Environ Sci Technol 38(8): 2435-2442.

44. Berberidou C, Poulios I, Xekoukoulotakis NP, Mantzavinos D (2007) Sonolytic, photocatalytic and sonophotocatalytic degradation of malachite green in aqueous solutions. Appl Catal B Environ 74(1-2): 63-72.

45. Bejarano-Pérez NJ, Suárez-Herrera MF (2008) Sonochemical and sonophotocatalytic degradation of malachite green: the effect of carbon tetrachloride on reaction rates. Ultrason Sonochem 15(4): 612–617.

46. Moumeni O, Hamdaoui O (2012) Intensification of sonochemical degradation of malachite green by bromide ions. Ultrason Sonochem 19(3): 404-409.

47. Schmidt D, Shah D, Giannelis EP (2002) New advances in polymer/layered silicate nanocomposites. Curr Opin Solid State Mater Sci 6(3): 205–212.

48. Gupta VK, Kumar R, Nayak A, Saleh TA, Barakat MA (2013) Adsorptive removal of dyes from aqueous solution onto carbon nanotubes: a review. Adv Colloid Interface Sci 193-194: 24-34.

49. Gupta N, Kushwaha AK, Chattopadhyaya MC (2012) Adsorption studies of cationic dyes onto Ashoka (Saraca asoca) leaf powder. J Taiwan Inst Chem Eng 43(4): 604-613.

50. Saravanan R, Gupta VK, Prakash T, Narayanan V, Stephen A (2013) Synthesis, characterization and photocatalytic activity of novel Hg doped ZnO nanorods prepared by thermal decomposition method. J Mol Liq 178: 88-93.

51. Saravanan R, Prakash T, Gupta VK, Stephen A (2014) Tailoring the electrical and dielectric properties of ZnO nanorods by substitution. J Mol Liq 193: 160-165.

52. Iijima S (1991) Helical microtubules of graphitic carbon. Nature 354: 56-58.

53. Khani H, Rofouei MK, Arab P, Gupta VK, Vafaei Z (2010) Multi-walled carbon nanotubes-ionic liquid-carbon paste electrode as a super selectivity sensor: application to potentiometric monitoring of mercury ion(II). J Hazard Mater 183(1-3): 402-409.

54. Salleh MAM, Mahmoud DK, Karim WA, Idris A (2011) Cationic and anionic dye adsorption by agricultural solid wastes: a comprehensive review. Desalination 280(1-3): 1-13.

55. Odom TW, Huang JL, Kim P, Lieber CM (1998) Atomic structure and electronic properties of single-walled carbon nanotubes. Nature 391(6662): 62-64.

56. Rajabi M, Mirza B, Mahanpoor K, Mirjalili M, Najafi F, et al. (2016) Adsorption of malachite green from aqueous solution by carboxylate group functionalized multi-walled carbon nanotubes: determination of equilibrium and kinetics parameters. J Ind Eng Chem 34: 130-138.

57. Shirmardi M, Mahvi A, Hashemzadeh B, Naimabadi A, Hassani G, et al. (2013) The adsorption of malachite green (MG) as a cationic dye onto functionalized multi walled carbon nanotubes. Korean J Chem Eng 30(8): 1603-1608.

58. Kiani G, Dostali M, Rostami A, Khatae AR (2011) Adsorption studies on the removal of malachite green from aqueous solutions onto halloysite nanotubes. Appl Clay Sci 54(1): 34-39.

59. Buzea C, Pacheco II, Robbie K (2007) Nanomaterials and nanoparticles: sources and toxicity. Biointerphases 2(4): 17-71.

60. Judit E P (2013) Introduction to Polymer Chemistry: A Biobased Approach, Technology & Engineering A Biobased Approach: Order Department, DEStech Publications, Inc, U.S.A.

61. Lakouraj MM, Mojerlou F, Zare EN (2014) Nanogel and superparamagnetic nanocomposite based on sodium alginate for sorption of heavy metal ions. Carbohydr. Polym 106: 34-41.

62. Wang Z, Huang Y, Wang M, Wu G, Geng T, et al. (2016) Macroporous calcium alginate aerogel as sorbent for Pb2+ removal from water media. J. Environ. Chem. Eng 4(3): 3185-3192.

63. Godiya CB, Cheng X, Li DW, Chen Z, Lu XL (2019) Carboxymethyl cellulose/polyacrylamide composite hydrogel for cascaded treatment/reuse of heavy metal ions in wastewater. J Hazard Mater 364: 28-38.

64. Wessling B (2010) New Insight into Organic Metal Polyaniline Morphology and Structure. Polymers 2(4): 786-798.

65. Yin X, Chung HT, Martinez U, Lin L, Artyushkova K, et al. (2019) PGM-Free ORR Catalysts Designed by Templating PANI-Type Polymers Containing Functional Groups with High Affinity to Iron. Journal of the Electrochemical Society 166 (7): 3240-3245.

66. Majid N (2015) Chapter Fourteen - Surface Area: Brunauer–Emmett–Teller (BET). Academic Press. Progress in filteration and separation 14: 585-608.

67. Adegoke KA, Bello OS (2015) Dye sequestration using agricultural wastes as adsorbents. Water Resour Ind 12: 8-24.

68. Asilturk M, Sayılkan F, Arpaç E (2009) Effect of Fe3+ ion doping to TiO2 on the photocatalytic degradation of malachite green dye under UV and vis-irradiation. J Photochem Photobiol Chem 203(1): 64-71.

69. Dawood S, Sen TK (2014) Review on dye removal from Its aqueous solution into alternative cost effective and non-conventional adsorbents. J Chem Process Eng 1: 1-7.

70. Sarkar AK, Pal A, Ghorai S, Mandre NR, Pal S (2014) Efficient removal of malachite green dye using biodegradable graft copolymer derived from amylopectin and poly(acrylic acid). Carbohydr Polym 111: 108-115.

71. Sartape AS, Mandhare AM, Jadhav VV, Raut PD, Anuse MA, et al. (2015) Removal of malachite green dye from aqueous solution with adsorption technique using Limonia acidissima (wood apple) shell as low cost adsorbent. Arab J Chem. 10(2): 3229-3238.

72. Savva I, Marinica O, Papatryfonos CA, Vekas L, Theodora KC (2015) Evaluation of electrospun polymer–Fe3O4 nanocomposite mats in malachite green adsorption. RSC Adv 5(21): 16484-16496.